Nonlinear generation of a zero group velocity mode in an elastic plate by non-collinear mixing

Pierric Mora [a,b,*], Mathieu Chekroun [a], Samuel Raetz [a], Vincent Tournat [a]

[a] *Laboratoire d'Acoustique de l'Université du Mans (LAUM), UMR 6613, Institut d'Acoustique - Graduate School (IA-GS), CNRS, Le Mans Université, France*
[b] *GERS-GeoEND, Univ Gustave Eiffel, IFSTTAR, F-44344 Bouguenais, France*

ARTICLE INFO

ABSTRACT

Zero Group Velocity (ZGV) modes are peculiar guided waves that can exist in elastic plates or cylinders, and have proved to be very sensitive tools in characterizing materials or thickness variations with sub-percent accuracy at space resolutions of about the plate thickness. In this article we show theoretically and experimentally how such a mode can be generated as the sum-frequency interaction of two high amplitude primary waves, and then serve as a local probe of material non-linearity. The solutions to the phase matching condition, *i.e.* condition for a constructive non-linear effect, are obtained numerically in the mark of classical, quadratic non-linearity. The coupling coefficients that measure the transfer rate of energy as a function of time from primary to secondary modes are derived. Experiments are conducted on an aluminum plate using piezo-electric transducers and a laser interferometer, and explore the interaction for incident symmetric and anti-symmetric fundamental Lamb modes. In an experiment operated without voltage amplifier we demonstrate that the resonant nature of these ZGV modes can be leveraged to accumulate energy from long excitations and produce detectable effects at extraordinarily low input power even in such weakly non-linear material.

1. Introduction

Nonlinear ultrasonics in non-destructive testing has received considerable interest in the last decades owing to its promise to detect material degradation at much earlier stages than linear techniques do [1].

As one among other non-linear effects that have shown great sensitivity to micro-structural changes, harmonic generation is often the ground of a strategy to interrogate a medium [2]. In this context, appealing guided wave based techniques have emerged [3–6], although their development has been hindered by the complexity of wave propagation in these structures which adds to the other difficulties that any non-linear based method must cope with. Indeed, due to dispersion, the phase matching condition without which no significant magnitudes are attained is in general not fulfilled for collinear interaction, except at some very specific combinations of modes and frequencies that have to be carefully identified [7,8], and among which only few are at reach in practice given the state of the art in transduction.

In an attempt to broaden the design space of this class of methods, recent works have begun to explore the new possibilities offered by non-collinear mixing [9–13]. Non-collinear mixing is the name given to the phenomenon of harmonic generation when the two primary waves come from different directions. Although well known [14–17]

and with identified advantages applied in non-destructive evaluation in the case of bulk waves (see *e.g.* [18,19]), and despite pioneer experimental demonstrations in plates in the 70s [20,21], this effect has remained out of focus for Lamb waves until the articles cited above. The benefits of non-collinear mixing are in general that it allows an easier separation between system and sample non-linearity. In the case of guided waves, the other benefit is that the solutions to the phase matching condition are tremendously more numerous, allowing most modes to be generated by a well chosen pair of primary waves. We show in this article how a zero group velocity mode can be excited this way.

Waves having zero group velocity (ZGV) and non-zero wavenumber can exist in elastic waveguides. They behave like thickness resonances although, due to their finite wavelength (about the plate thickness), they remain strongly localized in space and can serve as local probes of sample properties (*e.g.* defects [22], thickness changes [23–26], mechanical constants [27–30], bonding [31–33]) with a single point measurement. Owing to their high quality factor, these modes are usually relatively easy to generate and can be detected at great precision with non-contact setups. For instance, $Q \approx 15000$ was reported [23] in aluminum alloys, which enabled detecting and mapping [23,24] relative thickness variations as small as 2×10^{-4}. Successful applications

---

* Corresponding author at: GERS-GeoEND, Univ Gustave Eiffel, IFSTTAR, F-44344 Bouguenais, France.
  E-mail address: pierric.mora@univ-eiffel.fr (P. Mora).

in non-destructive testing were reported with air-coupled transducers in the $150 - 250$ kHz range [22], or with laser ultrasonics from MHz [23–31,33–36] to GHz [32] frequencies, covering thicknesses down to bonded nanostructures [32]. One noticeable exception to the contact-less detection that is usually required is found in civil engineering (the "impact-echo" technique [37]) where, due to the small size of the sensors regarding the thickness of the walls being probed, contact detection can be meaningful without significantly affecting the modes. Lastly, let us also mention that ZGV modes have led to the design of high-Q micro resonators, either optical [38] or mechanical [39] for electroacoustic components. Insights on the ranges of existence of ZGV modes as a function of Poisson's ratio can be found in Ref. [34]. Other aspects have been discussed such as the influence of boundary conditions and layering [40], anisotropy [28], or their time decay behavior due to dispersion and material damping [35].

Altogether, these qualities make ZGV modes attractive candidates to achieve new performances in evaluating the non-linear properties of a medium or a bonded assembly [41–43]. However — except from Ref. [44] which explores theoretically self-action effects in the mark of hysteretic non-linearity — reported works cover only linear properties. One obstacle regarding harmonic generation is that it is in general not possible to find a primary mode that collinearly satisfies the phase matching condition with a ZGV mode as target. The natural way to overcome this difficulty is to resort to non-collinear mixing. This is the starting point of the present article.

Let us give a brief illustration before going into details. Fig. 1 shows a setup in which two narrow-banded, high amplitude wave trains are launched in an aluminum plate in such a way that their wavevectors and frequencies sum to a ZGV point of the plate. After an interaction time of half a hundred cycles, the remaining field has a clear component at the expected ZGV frequency.

This article is organized as follows. We first obtain the solutions to the phase matching condition considering the "sum frequency" interaction and the so-called S_1S_2 ZGV mode as target. This mode is the lowest frequency and most widely known and exploited ZGV mode that is supported by plates in a very wide range of Poisson's ratio, covering most engineering isotropic materials (metals, concrete, plastics, *etc.*). We also derive and discuss the coefficients that quantify the interaction between selected modes. We then describe experimental realizations, the first two of which giving evidence of the phenomenon for different choices in the primary modes. Finally, a third experiment emphasizes one of the unique benefits that a ZGV mode can provide by demonstrating detectable effects obtained at low driving amplitudes.

2. Theoretical background

2.1. General considerations

We recall here a few background results of non-collinear harmonic generation in hyperelastic materials showing classical, quadratic non-linearity. These results can be obtained by considering the equations of motion for finite amplitudes in the perturbative approximation. They were first derived for bulk waves [14–17] and are qualitatively similar for guided waves [9,10] as the methodology to establish them extends naturally. Non-collinear mixing is also possible for other types of non-linearities, although it involves other angles, admissible symmetry pairings and harmonic orders — see Ref. [45] for bulk waves and hysteretic quadratic non-linearity. Contact acoustics non-linearity, another family of non-classical non-linearities, could also be relevant in the future in the case of the non-linear and non-collinear interactions at a crack [13,46].

Let us consider two primary displacement fields $\mathbf{u}_1$ and $\mathbf{u}_2$ propagating in a plate made of such a material. $\mathbf{u}_1$ and $\mathbf{u}_2$ are assumed to be monochromatic and composed of a single Lamb mode each:

$$\mathbf{u}_1 = \mathrm{Re}\left(A_1 \mathbf{U}_1(z)e^{i(\omega_1 t - \mathbf{k}_1^T \mathbf{x})}\right), \tag{1a}$$

Table 1
Material constants representative of several aluminum alloys. The third order moduli were determined by R. T. Smith et al. [47] from acoustoelastic measurements.

Density	Lamé's		Murnaghan's			
ρ	λ	μ	l	m	n	
2.7 g/cm³	58	24	−311	−401	−408	GPa
			−224	−237	−276	
			−202	−305	−300	
			−388	−358	−320	
			−337	−395	−436	

$$\mathbf{u}_2 = \mathrm{Re}\left(A_2 \mathbf{U}_2(z)e^{i(\omega_2 t - \mathbf{k}_2^T \mathbf{x})}\right), \tag{1b}$$

where the coordinate system $\mathbf{x} = (x, y, z)^T$ is such that the free surfaces of the plate are parallel to the (x, y) plane, and with the convention $\omega_1 \geq \omega_2 > 0$. The wave vectors $\mathbf{k}_i$ are contained in the (x, y) plane. Both pairs $(\omega_i, \mathbf{k}_i)$ satisfy the dispersion relations of the plate and are associated with mode shapes $\mathbf{U}_i$. From the non-linear interaction between $\mathbf{u}_1$ and $\mathbf{u}_2$ in the region where they intersect, small secondary waves are produced whose amplitudes are proportional to the product A_1A_2. If furthermore $(\omega_1, \mathbf{k}_1)$ and $(\omega_2, \mathbf{k}_2)$ satisfy the phase-matching condition, that is, if their sum or difference

$$\omega_3 = \omega_1 \pm \omega_2, \tag{2a}$$

$$\mathbf{k}_3 = \mathbf{k}_1 \pm \mathbf{k}_2, \tag{2b}$$

is such that $(\omega_3, \mathbf{k}_3)$ satisfies the dispersion relations of the plate, then one mode,[1] called $\mathbf{u}_3$, emerges from the secondary field. Its amplitude grows in proportion with the interaction time t:

$$\mathbf{u}_3 = \mathrm{Re}\left(A_3(t)\mathbf{U}_3(z)e^{i(\omega_3 t - \mathbf{k}_3^T \mathbf{x})}\right), \tag{3a}$$

$$A_3(t) = A_1 A_2\, \gamma_{1,2,3}^{(t)}\, t, \tag{3b}$$

with $\mathbf{U}_3$ the mode shape related to $(\omega_3, \mathbf{k}_3)$, and $\gamma_{1,2,3}^{(t)}$ a coupling constant which depends on the triplet of modes and on the elastic constants of the material — a derivation is given in Appendix A. In Eqs. (2), "+" and "−" signs correspond respectively to the "sum" and "difference" interactions (A_2 must be replaced by its conjugate A_2^* for the "−" case). Eq. (3b) is often written as a function of the propagation distance. Here the choice of the time variable is made necessary by the ZGV modes in which we are ultimately interested, which, because of their zero power flux, would otherwise yield infinite terms.

The coupling constants $\gamma_{123}^{(t)}$ are zero when triplets of inadequate symmetries are involved, prohibiting several families of interactions. A complete discussion can be found in [9,10]. For our specific case of a target of P-SV symmetric type, the possible combinations are those of two antisymmetric or two symmetric modes, regardless their belonging to the P-SV or SH families.

2.2. System under interest

From here on in this theoretical section we consider a plate made of a homogeneous and isotropic material, of thickness h (see Fig. 2-d). The material is modeled using elastic constants characteristic of aluminum (see Table 1). For such Poisson's ratio ($\nu = 0.35$), the S_1S_2 ZGV mode (or merely "ZGV mode" for short) is around $(\omega_{ZGV}, k_{ZGV}) \approx (0.93c_s, 0.25) \times 2\pi/h$, with c_s the shear wave velocity.

---

[1] Note that there could in principle be more than one mode satisfying the phase-matching condition simultaneously. Such exceptional cases are not discussed here.
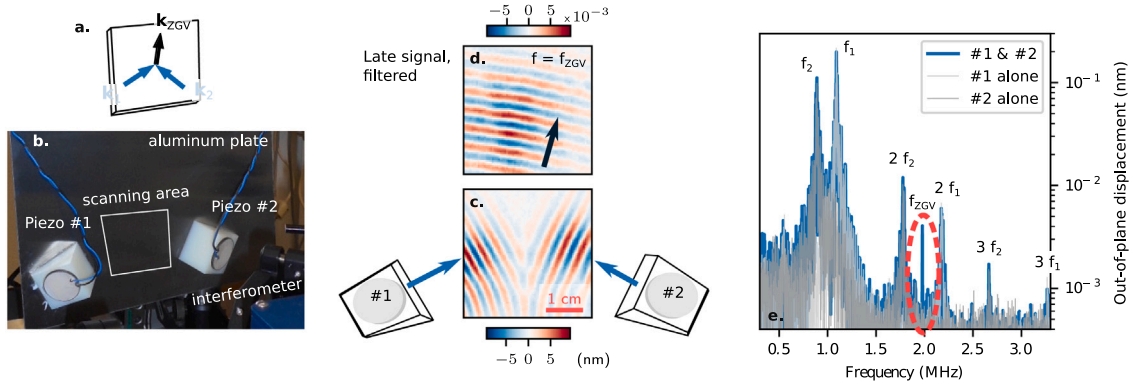
Fig. 1. (a) Schematic of the non-collinear interaction. (b) Photograph of the experimental setup. (c) Snapshot of the primary field arriving in the interaction region. (d) Fourier-transform of the field remaining after the interaction at the ZGV frequency. (e) Spectrum for piezos #1 and #2 activated alone or simultaneously.

Table 2
Frequency ranges and minimum interaction angles for mode pairs of admissible types giving solutions to the phase-matching condition for the generation of the $S_1 S_2$ ZGV mode as a sum interaction.

Primary modes	Frequency range (in units of $\frac{1}{2} f_{ZGV}$)	Min. angle
$S_0 - S_0$	63%–137%	127°
$A_0 - A_0$	73%–127%	155°
$SH_0 - SH_0$	73%–127%	149°
$S_0 - SH_0$	S_0: 92%–150%	139°
	SH_0: 50%–108%	
$A_0 - A_1$	A_0: 16%–70%	132°
	A_1: 130%–184%	
$A_0 - SH_1$	A_0: 41%–81%	144°
	SH_1: 119%–159%	

2.3. Phase matching condition

Here we seek the solutions to Eqs. (2) for the sum interaction when the target is the ZGV mode, *i.e.* $(\omega_3, \|\mathbf{k}_3\|) = (\omega_{ZGV}, k_{ZGV})$, and given a phase direction that is arbitrarily set along the y axis, *i.e.* $\mathbf{k}_3/\|\mathbf{k}_3\| = (0, 1, 0)^T$.

Methodology. We first numerically obtain (see *e.g.* [48]) the dispersion relations of the plate $\omega_n(k)$ and identify the modal branches that we want to be considered as primary fields: *e.g.* the S_0 branch for the $S_0 - S_0 \rightarrow$ ZGV case. We vary $\mathbf{k}_1$ on a square grid $[-k_{max}, k_{max}] \times [-k_{max}, k_{max}]$ whose bounds k_{max} are empirically set large enough to obtain all solutions. At each test point of the grid, $\mathbf{k}_2 = \mathbf{k}_3 - \mathbf{k}_1$ is deduced from Eq. (2b), and the sum angular frequency $\omega^+ = \omega_1(\|\mathbf{k}_1\|) + \omega_2(\|\mathbf{k}_2(\mathbf{k}_1)\|)$ is stored. Finally, a contour finder [49] (the *Marching squares* algorithm) is called to find the iso-values $\omega^+(\mathbf{k}_1) - \omega_3 = 0$ and returns the admissible $\mathbf{k}_1$ vectors, from which the corresponding admissible $\mathbf{k}_2$, angular frequencies ω_1 and ω_2, and interaction angles $\arccos(\mathbf{k}_1^T \mathbf{k}_2 / \|\mathbf{k}_1\| \|\mathbf{k}_2\|)$ can be post-treated.

Results. The methodology is applied to all possible primary pairings. The results for the three most canonical cases $A_0 - A_0 \rightarrow$ ZGV, $S_0 - S_0 \rightarrow$ ZGV and $SH_0 - SH_0 \rightarrow$ ZGV are represented in Fig. 2. Solutions are also found to the more exotic cases $S_0 - SH_0 \rightarrow$ ZGV, $A_0 - A_1 \rightarrow$ ZGV and $A_0 - SH_1 \rightarrow$ ZGV and are summarized in Table 2. Other combinations are either of wrong symmetry parity (*e.g.* $A_0 - S_0$ cannot generate a symmetric mode) or start at frequencies above the target.

Fig. 2-a represents (thick lines) the portions of the fundamental modal branches where the phase-matching condition can be satisfied by a non-collinear arrangement. Triangles mark the lowest and highest possible frequencies and correspond to a 180° interaction angle, while circles mark the case $f_1 = f_2$ where the interaction angle is minimal. Note that the interaction angle in this symmetric case can be easily

obtained by geometric considerations — it equals $2\arccos(c_1/c_3)$, with c_1 and c_3 the phase velocities of primary and secondary waves. The two ticks (blue line) correspond to $f_1, f_2 = \frac{1}{2} f_{ZGV} \pm 20\%$. Fig. 2-b represents the complete set of admissible primary wavevectors — it is actually the raw output of the contour finder. To help understanding, the wavevectors corresponding to the points marked in Fig. 2-a are drawn for the $S_0 - S_0 \rightarrow$ ZGV case. Finally, Fig. 2-c represents the angle that must be set between $\mathbf{k}_1$ and $\mathbf{k}_2$, as a function of the driving frequency f_1.

Closed-form approximate solution. Note that, because the dispersion of the A_0 and S_0 modes is small in the allowed frequency range, relatively good approximate results can be obtained by using the closed-form solution to non-collinear interaction of bulk waves of speed c_1 and c_3 with $c_1 \leq c_3$ — this solution is exact for the case of $SH_0 - SH_0 \rightarrow$ ZGV. The solution space of wavevectors is an ellipse with foci $\mathbf{0}$ and $\mathbf{k}_3$, with extreme values $\mathbf{k}_1 = \frac{1}{2}\mathbf{k}_3(1 \pm \frac{c_3}{c_1})$ at $\omega_1 = \frac{1}{2}\omega_3(1 \pm \frac{c_1}{c_3})$. Using this formula with the phase velocity of A_0 or S_0 taken at half the ZGV frequency predicts bounds of $\frac{1}{2} f_{ZGV} \pm 22\%$ (exact: $\pm 27\%$) for the $A_0 - A_0 \rightarrow$ ZGV interaction, and of $\frac{1}{2} f_{ZGV} \pm 44\%$ (exact: $\pm 37\%$) for the $S_0 - S_0 \rightarrow$ ZGV interaction.

2.4. Interaction coefficients

Here we give numerical values of the interaction coefficients $\gamma_{1,2,3}^{(t)}$ appearing in Eqs. (3b) and (A.12).

Normalization of the mode shapes. The coefficients $\gamma_{1,2,3}^{(t)}$ are defined up to a factor that depends on the normalization of the mode shapes $\mathbf{U}_i$. We choose to adopt a definition that allows a comparison with the well-known, scalar case of harmonic generation caused by two collinear longitudinal bulk waves. A detailed discussion of this choice is given in Appendix B. In a nutshell, we require the Lamb mode $\mathrm{Re}\left(A_i \mathbf{U}_i(z) e^{i(\omega t - \mathbf{k}^T \mathbf{x})}\right)$ to carry the same thickness-average mechanical energy as a plane bulk wave $A_i \cos \omega(t - x/c_i)$, leading to $\frac{1}{h} \int_0^h \|\mathbf{U}_i\|^2 \mathrm{d}z = 1$ for a homogeneous plate. We set the phase by requiring in-plane components to be pure real, with a non-negative value at $z = 0$ along the radial and azimuthal directions: $U_{i,x}|_{z=0} \geq 0$ (P-SV) and $U_{i,y}|_{z=0} > 0$ (SH) for $\mathbf{k}/\|\mathbf{k}\| = (1, 0, 0)^T$.

Generalized acoustic non-linear parameter. We introduce the following dimensionless coefficients to characterize the non-linear coupling within a given mode triplet:

$$\beta_{1,2,3} = \frac{2 A_3 c_l}{A_1 A_2 \omega_1 \omega_2 t}, \tag{4}$$

with c_l the longitudinal wave velocity. Eq. (4) is meant to be applied to measure $\beta_{1,2,3}$ from a time signal, under a plane wave assumption. When applied to bulk longitudinal waves with $\omega_1 \neq \omega_2$, $\beta_{1,2,3}$ coincides
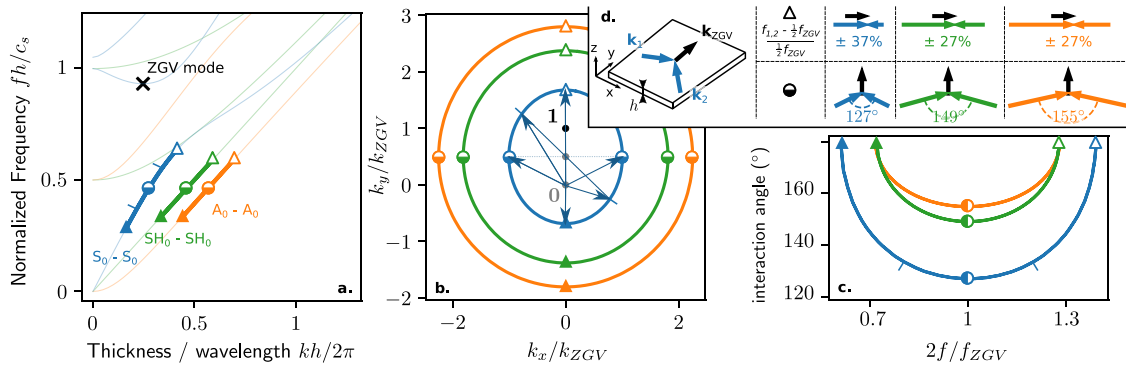
Fig. 2. Space of pairs $((f_1, \mathbf{k}_1); (f_2, \mathbf{k}_2))$ solutions to the phase matching condition for $S_0 - S_0 \rightarrow$ ZGV, $SH_0 - SH_0 \rightarrow$ ZGV and $A_0 - A_0 \rightarrow$ ZGV interactions. (a) Admissible frequency ranges (thick lines) superimposed on dispersion curves (thin lines). (b) Admissible wavevectors. Examples of pairs $(\mathbf{k}_1, \mathbf{k}_2)_{S_0}$ are drawn and the reflection across the point $\frac{1}{2}\mathbf{k}_{ZGV}$ relating them is represented by a thin dotted line. (c) Interaction angle as a function of the driving frequency of one of the two modes.

with the *acoustic parameter of quadratic non-linearity* β defined as a strain-hardening[2] factor $\sigma = \rho c_l^2 (\varepsilon + \beta \varepsilon^2)$, where σ is the stress, ε the strain, and $\beta = \frac{3}{2} + \frac{l + 2m}{\lambda + 2\mu}$. Eq. (4) can be related to material parameters using Eq. (3b), giving $\beta_{1,2,3} = 2\gamma_{1,2,3}^{(t)} c_l / \omega_1 \omega_2$. Furthermore, as $\gamma_{1,2,3}^{(t)}$ depends linearly on the Murnaghan's constants l, m, n, we can write:

$$\beta_{1,2,3} = \beta_{1,2,3}^{(0)} + \frac{\partial \beta_{1,2,3}}{\partial l} l + \frac{\partial \beta_{1,2,3}}{\partial m} m + \frac{\partial \beta_{1,2,3}}{\partial n} n. \tag{5}$$

The four coefficients that appear in the right-hand side of Eq. (5) depend only on the linear material constants (ρ, λ, μ) and on the triplet of modes. Comparing again to bulk longitudinal waves, one obtains $\beta^{(0)} = 3/2$, $\partial_l \beta = 1/(\lambda + 2\mu)$, $\partial_m \beta = 2/(\lambda + 2\mu)$ and $\partial_n \beta = 0$.

Conversion factor for measurements of the out-of-plane component. In this work the observable is the surface out-of-plane displacement $u_z|_{z=0}$. It is therefore convenient to use the alternative normalization (superscript $^{(z)}$) $\mathbf{u} = \mathrm{Re}\left(A_i^{(z)} \mathbf{U}_i^{(z)}(z) e^{i(\omega t - \mathbf{k}^T \mathbf{x})}\right)$ such that $U_{i,z}^{(z)}|_{z=0} = 1$ and $A_i^{(z)}$ is the measured amplitude. We call

$$\alpha_{1,2,3} = \left. \frac{U_{1,z} U_{2,z}}{U_{3,z}} \right|_{z=0} \tag{6}$$

the conversion factor to the former normalization such that Eq. (4) expresses as:

$$\beta_{1,2,3} = \alpha_{1,2,3} \frac{2 A_3^{(z)} c_l}{A_1^{(z)} A_2^{(z)} \omega_1 \omega_2 t}. \tag{7}$$

Results. The coefficients appearing in Eq. (5) are represented in Fig. 3 for the interactions $S_0 - S_0 \rightarrow$ ZGV, $A_0 - A_0 \rightarrow$ ZGV and $SH_0 - SH_0 \rightarrow$ ZGV, in the allowed frequency ranges. Selected numerical values are given in Table 3, along with the conversion factor (note that $\alpha_{1,2,3}$ is pure imaginary). The derivatives with respect to l, m and n are normalized by the P-wave modulus $\lambda + 2\mu$ to facilitate a comparison with β ($\beta = -5.1$ to -9.1 with our set of constants).

Let us explain on an example how to read Fig. 3. Suppose one wants to calculate the theoretical value of $\beta_{1,2,3}$ for the $S_0 - S_0 \rightarrow$ ZGV interaction, with equal primary frequencies $f_1 = f_2 = \frac{1}{2} f_{ZGV}$. Then, one has to read on Fig. 3-a at abscissa 1 the values of the solid (-1.44) and dashed curves (-2.40, -1.61, 0.31) — also reported in Table 3. These three latter values must then be multiplied respectively by l, m and n, and divided by $\lambda + 2\mu$. Finally, $\beta_{1,2,3}$ is obtained by summing these four values according to Eq. (5). Now, if one wants to calculate $\beta_{1,2,3}$ for another combination of primary frequencies, the procedure is similar but the curves must be read at another abscissa by taking either $f = f_1$ or $f = f_2$.
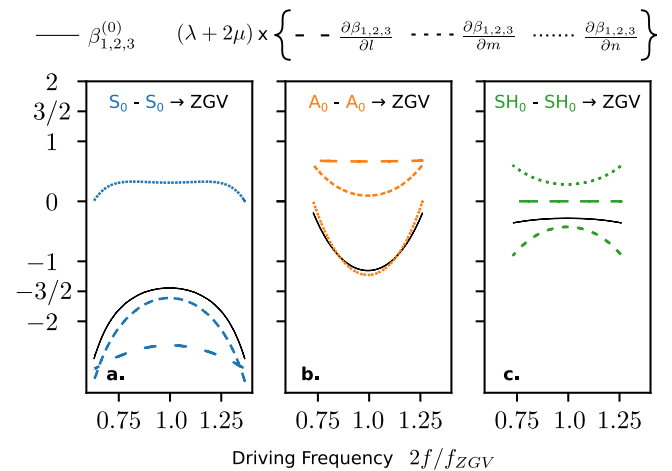
Fig. 3. Normalized non-linear coefficients for the three canonical combinations. The non-linear acoustic parameter $\beta_{1,2,3}$ can be obtained from a set of curves by applying Eq. (5).

As expected, these three interactions exhibit complementary sensitivities to l, m, n. As Murnaghan's constants are usually of the same sign, the $SH_0 - SH_0 \rightarrow$ ZGV interaction is the one with weakest transfer rate, because it depends on m and n with similar magnitudes but opposite signs and has zero component along l. On the other hand, the $S_0 - S_0 \rightarrow$ ZGV interaction sums contributions of l and m while it depends weakly on n, and is therefore the strongest one. The $A_0 - A_0 \rightarrow$ ZGV interaction, although somewhat weaker, is in turn interesting in that its relative sensitivities to the three constants change significantly with the frequency, such that, in principle, it seems possible to infer them all from experiments repeated at different driving frequencies and interaction angles. Another noteworthy characteristic of this interaction is that the geometric non-linear contribution $\beta_{1,2,3}^{(0)}$ is quite small at the extreme limits of the frequency range, *i.e.* for a 180° interaction angle: this point is the most sensitive choice to weak material non-linearities.
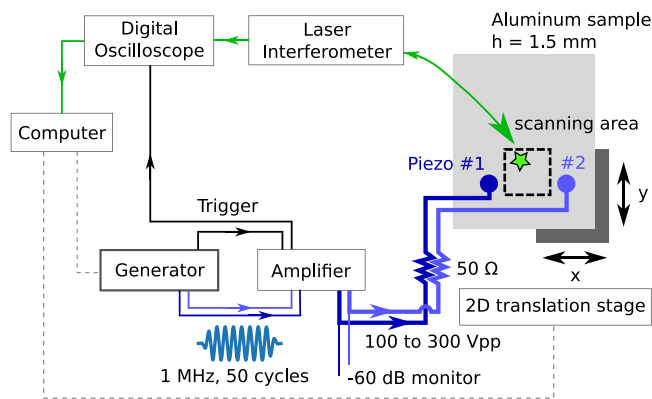
3. Experiments

Three experiments performed on a 1.5 mm thick aluminum plate (alloy Al 5754-H111, lateral dimensions 20×30 cm^2) are reported in the following sections. Prior to these experiments, the exact value of the $S_1 S_2$ ZGV resonance in the plate was determined using a classical experimental setup — we measured $f_{ZGV} = 1.98$ MHz.

Table 3

Selected theoretical values of the coefficients from which the non-linear acoustic parameter $\beta_{1,2,3}$ can be calculated, for the three canonical combinations, and of the conversion factor $\alpha_{1,2,3}$ for measurements of the out-of-plane displacement (see Eqs. (5) and (6)). Ranges for $\beta_{1,2,3}$ are min–max values from the sets of third order moduli given in Table 1 which represent different alloys.

Primary modes	Configuration	$\beta_{1,2,3}^{(0)}$	$(\lambda + 2\mu)\times$	$\left\{\dfrac{\partial\beta_{1,2,3}}{\partial l}\right.$	$\dfrac{\partial\beta_{1,2,3}}{\partial m}$	$\left.\dfrac{\partial\beta_{1,2,3}}{\partial n}\right\}$	$\alpha_{1,2,3}$	Typical $\beta_{1,2,3}$ in aluminum
$S_0 - S_0$	$f_1 = \frac{1}{2}f_{ZGV}$ $\langle \mathbf{k}_1, \mathbf{k}_2 \rangle = 127°$	-1.44		-2.40	-1.61	0.31	$-0.39\,i$	6.4 to 11.9
	$f_1 = \frac{1}{2}f_{ZGV} \pm 37\%$ $\langle \mathbf{k}_1, \mathbf{k}_2 \rangle = 180°$	-2.64		-2.80	-3.01	0	$-0.36\,i$	10.0 to 17.8
$A_0 - A_0$	$Lf_1 = \frac{1}{2}f_{ZGV}$ $\langle \mathbf{k}_1, \mathbf{k}_2 \rangle = 155°$	-1.15		0.66	0.10	-1.23	$-0.99\,i$	-0.2 to 1.4
	$f_1 = \frac{1}{2}f_{ZGV} \pm 27\%$ $\langle \mathbf{k}_1, \mathbf{k}_2 \rangle = 180°$	-0.19		0.68	0.73	0	$-1.0\,i$	-3.3 to -5.2
$SH_0 - SH_0$	$Lf_1 = \frac{1}{2}f_{ZGV}$ $\langle \mathbf{k}_1, \mathbf{k}_2 \rangle = 149°$	-0.28		0	-0.43	0.28		0.0 to 0.3
	$f_1 = \frac{1}{2}f_{ZGV} \pm 27\%$ $\langle \mathbf{k}_1, \mathbf{k}_2 \rangle = 180°$	-0.36		0	-0.90	0.60		0.1 to 0.9

Fig. 4. Schematic of the experimental setup common to Exps. #1 and #2. The primary field is generated by two contact transducers fed with high voltage. The surface out-of-plane displacement is recorded as a point detection over a 2D grid.

Setup. Fig. 4 represents the experimental setup that is common to Exps. #1 and #2, and of which Exp. #3 only slightly differs. Two independent tonebursts at frequencies f_1 and f_2 close to 0.99 MHz are sent by a signal generator (Tektronix AWG-3022C) into a high power gated amplifier (RITEC SNAP 5000), and then fed into piezoelectric disks (25 mm diameter, 2 mm thickness) glued on heads. The heads (wedges for Exps. #1 and #3, metallic footprints for Exp. #2, see Figs. 6-a and 7-a) are designed to select a desired Lamb mode and are themselves glued onto the aluminum plate. The plate is mounted on a 2D translation stage (Newport UTS50CC and SMC100CC) that can span 5 cm on each axis at micrometric precision. Waves are detected with a laser interferometer (Tempo 1D, Bossa Nova Technologies; bandwidth of $20\,\text{kHz} - 1\,\text{GHz}$) that measures the absolute out-of-plane displacement on a focused spot that is pointwise regarding the millimetric wavelenghts involved. This device is chosen for its very good sensitivity as well as for allowing non-contact detection, which is essential to detect a ZGV mode without dramatically affecting it. It has however a drawback in that it saturates for peak amplitudes above $5 - 6\,\text{nm}$, levels that are easily reached with our transducers when driven at amplified voltages. Digitization (PicoScope 5444D) is done on 15 bits at a 15 MHz sampling rate and signals are averaged 40 (for 2D scans) to 80 times (at single points) to improve the signal to noise ratio (SNR). The piezoelectric disks are operated near a thickness resonance and can hence be considered as narrow-band transducers. Experiments #1 and #2 operate at voltages about 200 Vpp (*i.e.* 100 W/channel) on 50 cycles, while Exp. #3 does not use the amplifier and operates at 20 Vpp (*i.e.* 1 W/channel) on 2000 cycles.

3.1. *Experiment* #1: $S_0 - S_0 \to$ ZGV

We report in this section a first experiment in which the ZGV mode is generated using the $S_0 - S_0 \to$ ZGV interaction.

Methodology. Wedges made of Nylon (type PA6) are manufactured to selectively excite the S_0 mode. Snell–Descartes' law (2.7 mm/μs for the longitudinal wave in Nylon, and 5.0 mm/μs phase velocity for the S_0 Lamb mode at 1 MHz) predicts an optimal angle of incidence of 33°. According to the predictions of Section 2.3, the wedges are glued on the plate to form an angle of 127°. The driving frequencies are set with a small difference to facilitate the distinction between input and sample non-linearity: $f_1 = 1.09$ MHz and $f_2 = 0.89$ MHz (*i.e.* ±10%). This small $|f_1 - f_2|/2$ does not affect significantly the interaction angle which is almost constant around $|f_1 - f_2|/2 = 0$ (see Fig. 2-c).

Results and discussion. Results are shown in Figs. 5 and 6.

A typical signal recorded at the center of the region where beams #1 and #2 cross is represented in Fig. 5-a. It consists of two parts. During the first tens of μs the interferometer detects the intense, primary S_0 field, and saturates — the inset shows in thinner line the actual amplitude reconstructed from an acquisition at lower driving voltage. For harmonics analysis, this first part is blind. Once the 50 cycles trains are gone, the interferometer detects a much lower field, most of which is linear and composed of unwanted, direct A_0 modes, and of a diffuse $A_0 + S_0$ field due to edges reflections. Fig. 5-b shows a time–frequency analysis of the signal. Different spectral contributions appear after the saturated part. Of those, $2f_1$, $2f_2$, $3f_1$ and $3f_2$ are thought to be mainly due to the wedge/plate and wedge/piezo adhesive bonds because they can vary from absent to strong when unmounting/remounting the wedges and repeating the measurement. The component at $f_1 + f_2 = 1.98$ MHz $= f_{ZGV}$ distinguishes from all others in that, besides being detectable only when both piezo are activated, it is much more monochromatic and of almost constant amplitude over long times — remember that 1000 μs represent nearly 2000 periods. This clearly indicates that we are observing the expected phenomenon. Fig. 5-c shows a spectrum of the non-saturated part of the signal (the time window is depicted in black in Fig. 5-a) together with spectra of #1 and #2 alone, allowing the previous remark to be appreciated more quantitatively. Then, Figs. 5-d to -g show how the peak amplitude at $f_1 + f_2$ varies along with several control parameters. One indeed observes a quadratic trend with the driving voltage (Fig. 5-d) and a linear trend with the number of cycles (Fig. 5-e). Fig. 5-f gives an idea of how sharp the effect is in matching $f_1 + f_2$ with f_{ZGV}, although strictly speaking the peak width depends also critically on the number of input cycles. The fact that no harmonics is generated for $f_1 + f_2 < f_{ZGV}$ is not surprising because the $S_1 - S_2$ branch is not propagative — and as such cannot accumulate energy over long excitations, and other interactions $S_0 - S_0 \to S_0, SH_0, A_0, SH_1, A_1$ are not

possible due to wrong symmetry pairings or absence of solution to the phase matching condition. However, as emphasized by the asymmetry of the peak, the side $f_1 + f_2 > f_{ZGV}$ requires another explanation. We think that several adverse features combine to this absence of detection, namely a window effect and two physical reasons to why higher frequencies should be generated with much less efficiency:

- as we are blind during forcing, we only observe whatever remains without traveling (the ZGV mode) or comes back as a smaller, diffuse field,
- the group velocity becomes significant, so the secondary wave soon leaves the interaction area without accumulating much energy,
- there is a strong mismatch in the phase matching condition: because the dispersion relation $f(k)$ is flat at k_{ZGV}, increasing slightly $f_1 + f_2$ means a large change on $\|\mathbf{k}_3\|$, and hence on the interaction angle.

Fig. 5-g shows a study on the influence of the difference $|f_1 - f_2|/2$. It can be seen that despite the relatively high level of input non-linearity observed at $|f_1 - f_2|/2 = 0$ (for which $2f_1 = 2f_2 = f_1 + f_2$, thus comprising second harmonic generation at $2f_1$ and $2f_2$ from each excited beam, and the non-collinear wave mixing effect $f_1 + f_2$ exciting the ZGV mode), the subtraction step (#1&#2) − #1 − #2 (red squares) is effective in recovering at good precision the true amplitude resulting only from the non-linear and non-collinear wave-mixing effect at $f_1 + f_2$ and allows to isolate the sample non linearity. We rely on this conclusion for Exp. #2 described in the following section.

Finally, (x, y) scans (4×4 cm^2 sampled in 64×64 points) are presented in Fig. 6 as space and wavenumber analyses. Fig. 6-b shows a snapshot of the primary field at early times, when arriving in the interaction region. Fig. 6-c shows the wavenumber-frequency content of the primary field at the driving frequencies, reconstructed from lower driving voltages to avoid saturation biases, and time windowed to select only the incident train. Theoretical dispersion relations are superimposed in thin colored circles to facilitate interpretation. Then, Figs. 6-d and -e show the late field (i.e. for $t > 120$ μs to exclude saturation) filtered at the ZGV frequency. When both piezos are active, the observed field is indeed dominated by the expected ZGV mode with an almost purely space-harmonic content, and is maximal at the location where the interaction occurred.

3.2. Experiment #2: $A_0 - A_0 \rightarrow ZGV$

We report in this section a second experiment that is similar to the previous one except that it explores the $A_0 - A_0 \rightarrow ZGV$ interaction.

Methodology. Comb type heads consisting of a smooth (top) and a machined (bottom) faces are manufactured in brass disks (see Fig. 7-a). Piezoelectric disks are glued on the smooth faces and operated near a thickness resonance. The machined faces are glued to the plate and transmit an out-of-plane excitation distributed in a pattern that matches a A_0 planar wavefront (2.6 mm at 1 MHz), thus selectively exciting this mode (see Fig. 7-b,c). The heads are oriented to form an angle of 155° between the preferential directions of the waves being generated, according to the predictions of Section 2.3. The rear surroundings of each transducer are covered with adhesive paste with the twofold purpose to dampen the strong specular rays coming from the neighboring edges, and to reduce the resonant behavior of the heads. Relying on the good promises of the subtraction processing (see Fig. 5-g), the driving frequencies are set equal: $f_1 = f_2 = 0.99$ MHz.

Results. Fig. 7 shows (x, y) scans of the wave field (4×4 cm^2 sampled in 80×80 points). For details in the interpretation, the reader is referred to the previous section and to the very similar Fig. 6. Here again, the detection of the ZGV mode resulting from the non-collinear interaction is demonstrated.

3.3. Measured non-linear acoustic parameters

The theoretical framework presented in Section 2.4 and Appendix A is restricted to plane waves. However, the experiments involve beams of finite width. The S_1S_2 ZGV mode is quite dispersive, and hence prone to diffraction attenuation. When generated by a brief point or line source such as a laser impact, diffraction dominates over material damping at early times, resulting in a fast $t^{-1/2}$ decay [35]. Here the context is somewhat different in that the interaction zone acts as a distributed source with a moving phase, but we do notice a dependence on the time window used to extract the ZGV amplitude. This dependence can be well observed in Fig. 8-f on the part labeled *free decay* — see Section 3.4.

There are two known ways to cope with diffraction and damping. The first and best way is to fit the observed space–time variations with a propagation model. It is well documented for collinear generation [2], however, methodological developments are still needed for non-collinear mixing. The second way is to use only the slope of the variations, taken as close to the source as possible. This is the approach retained here. Going back to Fig. 8-f, and also to Fig. 5-e, variations appear well linear over time segments of at least 50 μs, as the plane wave model predicts it. In a collinear setup this is a good indication that attenuation biases are limited on these scales.

Methodology. The ZGV amplitude is measured by time-windowing over 50 μs just after the interaction has ceased. For instance, the black window drawn in Fig. 5-a is replaced with a window going from 80 μs to 130 μs. The signals are then 3D-Fourier-transformed and $|A_3|$ is read at the ZGV frequency as the max value in the (k_x, k_y) space. The amplitudes $|A_1|$ and $|A_2|$ are obtained similarly by time-windowing to select the interaction (e.g. from 30 μs to 70 μs in Fig. 5-a), 3D-Fourier-transforming, and reading the max values at the driving frequencies f_1 and f_2. Finally, Eq. (7) is applied by taking $c_l = 6270$ m/s, $t = 50$ μs as excitation duration; $\omega_1 = \omega_2 = 2\pi \times 0.99$ MHz and $|\alpha_{1,2,3}| = 0.99$ for the $A_0 - A_0 \rightarrow ZGV$ case; $\omega_1 = 2\pi \times 0.89$ MHz, $\omega_2 = 2\pi \times 1.09$ MHz and $|\alpha_{1,2,3}| = 0.39$ for the $S_0 - S_0 \rightarrow ZGV$ case.

Results. We obtained $|A_1| = 8.9$ nm, $|A_2| = 5.4$ nm and $|A_3| = 13.4 \times 10^{-3}$ nm for the $S_0 - S_0 \rightarrow ZGV$ experiment, giving $|\beta_{S_0,S_0,ZGV}^{exp}| = 0.7$, and $|A_1| = 11.1$ nm, $|A_2| = 10.9$ nm and $|A_3| = 19.8 \times 10^{-3}$ nm for the $A_0 - A_0 \rightarrow ZGV$ experiment, giving $|\beta_{A_0,A_0,ZGV}^{exp}| = 1.1$. Compared to the plausible values estimated in the theoretical analysis $\beta_{S_0,S_0,ZGV}^{th} = 6.4$ to 11.9 and $\beta_{A_0,A_0,ZGV}^{th} = -0.2$ to 1.4 (see Table 3), the agreement is very good for the $A_0 - A_0 \rightarrow ZGV$ experiment while it is bad for the $S_0 - S_0 \rightarrow ZGV$ one. We currently lack a satisfactory explanation, although finite-beam effects could have been naively discarded despite the justification given above, and although this comparison is only indicative because the model material constants (l, m, n) represent other aluminum alloys.

3.4. Experiment #3: generation at low amplitudes

Methodology. We go back to the $S_0 - S_0 \rightarrow ZGV$ interaction and use the same setup as for Exp. #1, except that the amplifier is now removed (see Fig. 8-a). The outputs of the signal generator are directly connected to the piezoelectric disks (with 50 Ω loads) glued on the wedges. The driving frequencies f_1 and f_2 are set with a small difference $f_2 - f_1 = 10$ kHz (i.e. $\pm 0.5\%$) around half the ZGV frequency. The generator is able to deliver up to 20 Vpp into 50 Ω on each channel. Compared to Exp. #1, the input voltages are lower by a factor of roughly 10. Non-linearly generated amplitudes are then expected to be reduced by a factor of ≈ 100. To compensate these lower levels, we increase the number of cycles from a few tens to 2000 (i.e. $\approx \times 40$). This clearly does not balance the drop entirely, but proves to generate amplitudes high enough to be unambiguously detected with a few tens averages.
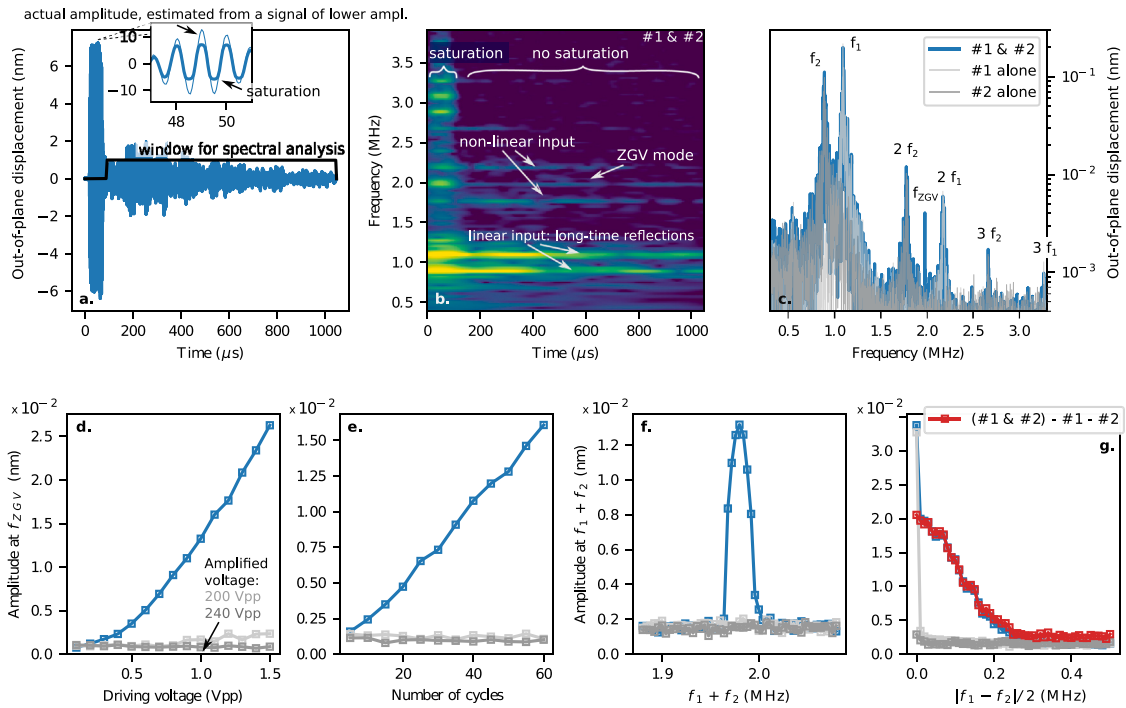
Fig. 5. Typical signals at the center of the crossing region for the $S_0 - S_0 \rightarrow$ ZGV interaction. (a) Time signal. (b) Time–frequency analysis. (c) Spectrum of the non-saturated part ($t > 120$ μs) for piezos #1 and #2 activated alone or simultaneously. (d, e, f, g) Peak amplitude at the sum frequency when varying (d) the driving voltage of both piezos, (e) the number of cycles of the tonebursts, (f) the sum frequency $f_1 + f_2$ while keeping constant $(f_1 - f_2)/2 = 0.1$ MHz, (g) the difference $|f_1 - f_2|/2$ while keeping constant $f_1 + f_2 = 1.98$ MHz.
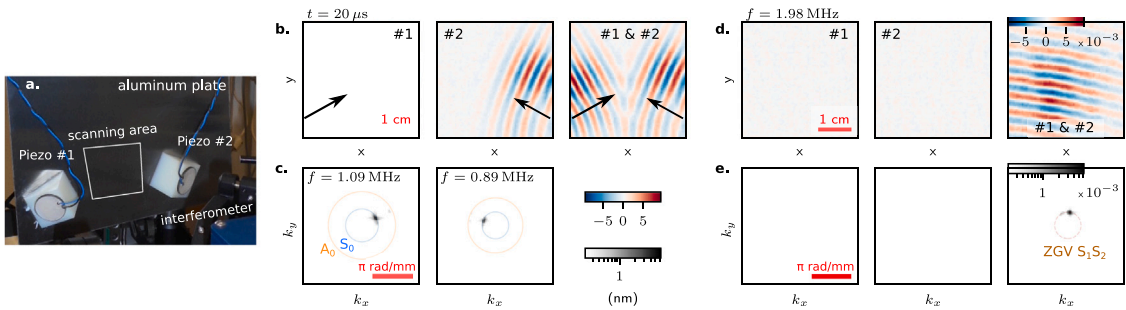
Fig. 6. 2D view of the $S_0 - S_0 \rightarrow$ ZGV interaction. (a) Photograph of the setup showing the wedge transducers and the laser interferometer. (b) Snapshot of the primary field arriving in the interaction region. (c) Wavenumber content of the primary field at the driving frequencies. (d) Real part of the field at the ZGV frequency (windowed to $t > 120$ μs to exclude saturation, see Fig. 5-a). (e) Wavenumber content of (d).
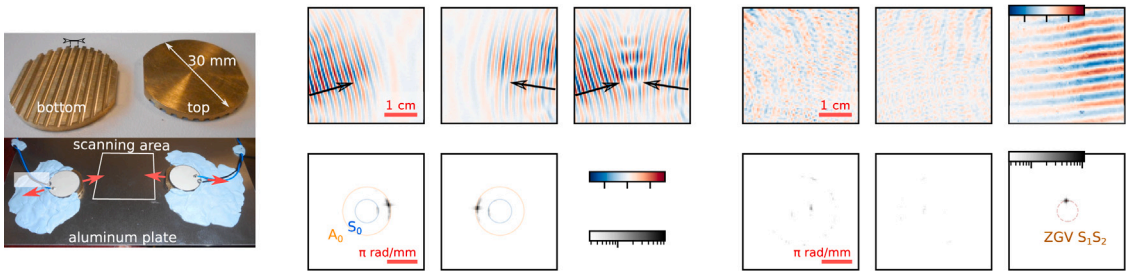
Fig. 7. 2D view of the $A_0 - A_0 \rightarrow$ ZGV interaction. (a) Photograph of the setup showing the brass heads with A_0-like footprints, with red arrows representing outgoing waves. (b) Snapshot of the primary field arriving in the interaction region. (c) Wavenumber content of the primary field at the driving frequencies. (d) Real part of the field at the ZGV frequency (windowed to $t > 120$ μs to exclude saturation, see Fig. 5-a). (e) Wavenumber content of (d).

Results and discussion. The results presented in Fig. 8 were recorded with 50 averages. Because of the lower amplitudes, the interferometer no longer saturates during excitation. This makes this early stage fully observable and enables a more complete picture.

Fig. 8-b shows a few snapshots of the field (real part) during and after excitation with a time–frequency processing centered at the ZGV frequency. One can clearly see that a wave pattern progressively appears until $t = 2000$ μs, that is, when the excitation stops, and then vanishes. Fig. 8-c shows a typical signal recorded at the center of the observation window, with a peak amplitude about 0.8 nm when both transducers are emitting. The beatings in the first 2000 μs are due to the small difference between the driving frequencies. The spectrum of this entire signal is shown in Fig. 8-d: as emphasized by the inset around 2 MHz no peaks are measured at $2f_1$ or $2f_2$, meaning that the non-linearity of the receiving system is now indeed too small to be observed. The peak at $f_1 + f_2$ (1.8 10^{-3} nm peak amplitude) has, in turn, a SNR of about 20 dB. The same signal is then shown in Fig. 8-e in a time–frequency representation, with a focus on the ZGV frequency — the magnitude at the driving frequencies is also plotted in gray lines. A tendency of linear increase with time can indeed be observed during forcing, followed by a slow, free decay. Finally, Fig. 8-f shows the same time–frequency analysis applied to the data transformed into the wavenumber domain $(x, y) \rightarrow (k_x, k_y)$. The black line represents the magnitude of the point $(f_{ZGV}, \mathbf{k}_{ZGV})$ as a function of time, while gray lines show the values at neighboring points (the solid/dashed curves stand for minus/plus a given percentage in the wavenumber k). The time dependence can this way be observed more accurately — the Fourier transform on 64×64 points can improve the SNR by up to $+36$ dB for a pure harmonic pattern. One can now observe a trend towards saturation in the growth. It is also noteworthy that the decay rate results faster for greater (dashed lines) than for smaller (solid lines) wavenumbers. An explication could be that greater wavenumbers are indeed more dispersive than smaller ones, although it is not clear to us whether viscous attenuation also contributes quantitatively to this difference.

Before closing this section, we should not disregard the fact that the very attractive prospects offered by this low power setup come at the cost of technical difficulties that are common to resonance experiments. Indeed, the price to pay is that the driving frequencies must be adjusted with extreme care, because a target error of one part over 2000 (the number of cycles) now significantly degrades the phase matching condition. Such required accuracy starts to be sensitive to temperature effects: this was not an issue for scans running over a couple hours, but we did observe variations with overnight fluctuations (about $\pm 2°$ in the room). Another limitation could be attenuation. Here the large number of cycles was still well below the quality factor of the ZGV mode, which often exceeds 10^4 in metal plates, so that even more cycles would have yielded higher amplitudes. But in more dissipative media, compensating low amplitudes with long excitations is obviously a more limited strategy.

4. Conclusion

The non-linear generation of the S_1S_2 ZGV Lamb mode at the intersection of two high amplitude beams of lower frequency has been analyzed theoretically and experimentally in an aluminum plate. The methodology followed can be transposed to other materials, to the difference interaction, and to other targeted modes. A new derivation of the coupling coefficients was given that is suited to an observation of the interaction as a function of time, and is thereby adapted to zero group velocity modes. Theoretical values of these coefficients were discussed for the most canonical cases. The experimental realizations involved the fundamental symmetric and antisymmetric Lamb modes, which are relatively easy to excite selectively and efficiently. A complete space–time observation of the phenomenon was achieved in an experiment operated at low power, from the emergence of the mode during forcing to its free decay. The main features of the interaction were observed, such as non-trivial interaction angle, quadratic dependence with the driving voltage, or linear dependence with the number of excitation cycles.

In the context of harmonic generation, the specificity of zero group velocity modes is that energy can be accumulated by simply launching longer primary waves into an intersection area whose diameter can be as small as a few plate thicknesses. In contrast, in configurations that produce propagating modes, accumulating energy requires to increase the interaction area, which dilutes information and soon faces trivial limitations related to the geometrical constraints of the actual system. Taking advantage of this appealing property, we showed that targeting such a mode enables to generate detectable non-linear effects using input powers up to two orders of magnitude lower than when targeting other modes.

Zero group velocity modes appear as promising tools based on which novel non-destructive characterization methods can be developed to assess locally the non-linear properties of a plate. Among possible applications, we believe that they could be relevant to evaluate the bonding quality of an adhesive joint. They could also be a route to achieve harmonic generation with a fully non-contact system using a time-modulated laser excitation.

Codes availability

Python programs for finding solutions to the phase-matching condition and for obtaining theoretical values of the non-linear parameter are available upon request.

Declaration of competing interest

The authors declare that they have no known competing financial interests or personal relationships that could have appeared to influence the work reported in this paper.

Acknowledgments

## Appendix A. Derivation of the interaction coefficients

The interaction coefficients appearing in Eq. (3b) are usually derived in the literature in the frequency domain, by expanding in a modal series the small wave field resulting from the non-linear interaction. Here, we take a slightly different approach in that the modal series is expressed in the wavenumber domain to allow for an analytical treatment of the time variable. Indeed, this time-domain resolution is necessary because Zero Group Velocity modes yield singularities when viewed in the frequency domain — their forced response grows unbounded with time as energy accumulates without traveling.

We start by briefly recalling the equations of motion for finite amplitudes in a waveguide as they can be established in the perturbative approximation. More details can be found in e.g. [50–52] for the collinear case, and in [6,9] for a formalism more suited to the non-collinear case.

Let $\mathbf{x} = (x, y, z)^T$ refer to the so called "natural" coordinates, i.e. attached to the system at rest. The system under interest is a traction-free plate that is unbounded in the (x, y) plane and comprised between $z = 0$ and $z = h$ (see Fig. 2-d). Two wave trains of finite amplitude, labeled #1 and #2 further on, are generated within the plate. We call $\mathbf{u}(\mathbf{x})$ the total displacement field produced by these waves and their interaction. Perturbation theory starts by expanding $\mathbf{u}$ as a sum of terms of different order:

$$\mathbf{u} = \mathbf{u}_1 + \mathbf{u}_2 + \mathbf{u}_{11} + \mathbf{u}_{22} + \mathbf{u}_{12}, \tag{A.1}$$
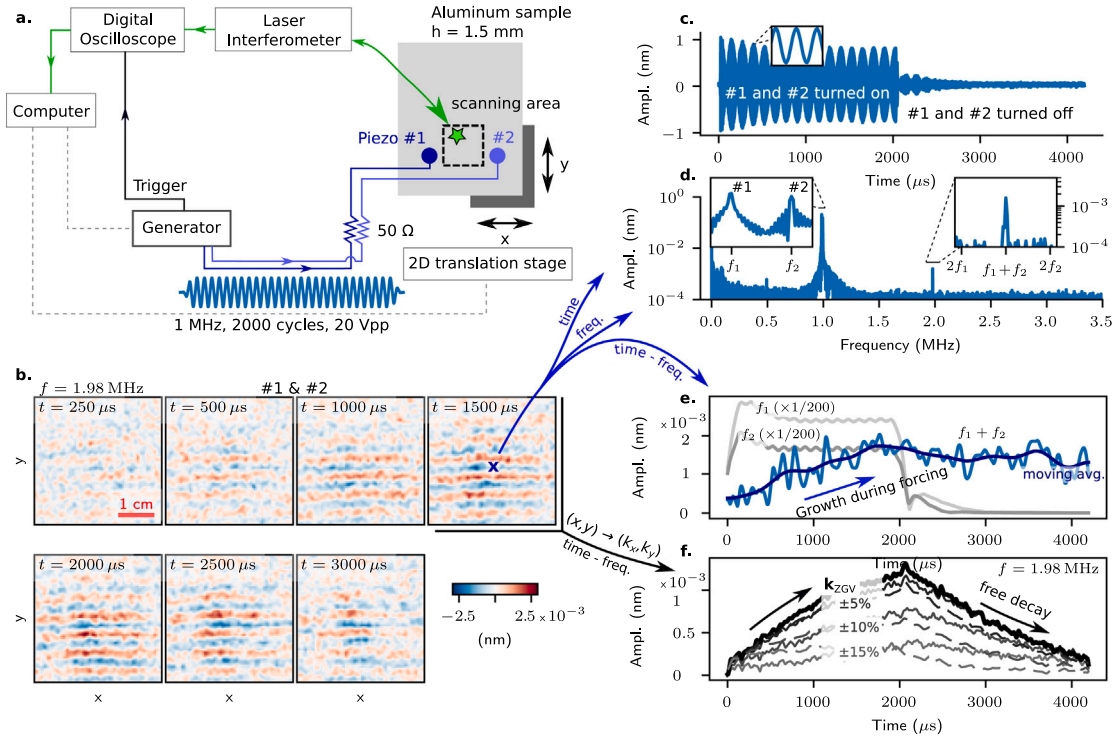
Fig. 8. Low power generation of the $S_0 - S_0 \rightarrow$ ZGV. (a) Schematic of the experimental setup (Exp. #3). (b) Snapshots of the field (real part) at the ZGV frequency processed with a time–frequency filter. (c) Typical signal (out-of-plane displacement). (d) Spectrum of (c) (entire signal). (e) Time–frequency analysis of (c) at the ZGV frequency (blue) and at the driving frequencies (grays). (f) Time–frequency analysis in the wavenumber domain at the ZGV frequency: at $\mathbf{k} = \mathbf{k}_{ZGV}$ (black), $\mathbf{k} = \mathbf{k}_{ZGV}(1-\text{pct})$ (solid grays) and $\mathbf{k} = \mathbf{k}_{ZGV}(1+\text{pct})$ (dashed grays).

where $\mathbf{u}_1$ and $\mathbf{u}_2$ (order 1) denote the primary fields, and $\mathbf{u}_{11}$, $\mathbf{u}_{22}$ and $\mathbf{u}_{12}$ (order 2) denote fields resulting from non-linear interactions: $\mathbf{u}_{11}$ refers to the self-interaction of wave #1, $\mathbf{u}_{22}$ to the self-interaction of wave #2, and $\mathbf{u}_{12}$ to the mutual interaction of waves #1 and #2. Note that $\mathbf{u}_{12}$ is the same as $\mathbf{u}_3$ in Section 2.1 when the phase matching condition is satisfied and a single mode dominates. We shall focus only on this latter term further on. For $\mathbf{u}_{12}$, the balance of forces and boundary conditions read, in absence of external load:

$$\rho \partial_t^2 \mathbf{u}_{12} - \mathbf{div}\, \mathbf{S}_L(\mathbf{u}_{12}) = \mathbf{f}_{vol}, \tag{A.2a}$$

$$\mathbf{S}_L(\mathbf{u}_{12}) \cdot \mathbf{n}_z = \mathbf{f}_{surf} \quad \text{for } z = 0, h. \tag{A.2b}$$

In Eqs. (A.2) $\mathbf{n}_z$ is the unit vector along the z axis, oriented upwards, and $\mathbf{S}_L(\mathbf{u}_{12}) = \mathbf{C} : \nabla \mathbf{u}_{12}$ is the linear part of the first Piola–Kirchhoff stress tensor referring to $\mathbf{u}_{12}$, with $\mathbf{C}$ the 4th-rank stiffness tensor. The source terms appearing in the right hand side are $\mathbf{f}_{vol} = \mathbf{div}\, \mathbf{S}_{NL}(\mathbf{u}_1, \mathbf{u}_2, 2)$ and $\mathbf{f}_{surf} = -\mathbf{S}_{NL}(\mathbf{u}_1, \mathbf{u}_2, 2) \cdot \mathbf{n}_z$, with $\mathbf{S}_{NL}(\mathbf{u}_1, \mathbf{u}_2, 2)$ the non-linear part of the first Piola–Kirchhoff stress tensor of the total field $\mathbf{u}$ that gathers products between $\nabla \mathbf{u}_1$ and $\nabla \mathbf{u}_2$ (the last argument $\varepsilon 2\varepsilon$ emphasizes the truncation order).

We assume that the material is hyperelastic, with a classical, quadratic non-linear component. In the case of an isotropic medium, the elastic energy density function can be written as:

$$\mathcal{W} = \frac{\lambda}{2}\text{tr}(\mathbf{E})^2 + \mu\text{tr}(\mathbf{E}^2) + \frac{A}{3}\text{tr}(\mathbf{E}^3) + B\text{tr}(\mathbf{E})\text{tr}(\mathbf{E}^2)$$
$$+ \frac{C}{3}\text{tr}(\mathbf{E}^3) + O(\mathbf{E}^4). \tag{A.3}$$

In Eq. (A.3) $\mathbf{E} = \frac{1}{2}[\nabla \mathbf{u} + \nabla \mathbf{u}^T + \nabla \mathbf{u}^T \nabla \mathbf{u}]$ is the Lagrangian strain tensor, λ and μ are Lamé's constants, and A, B and C are Landau and Lifshitz's third order elastic constants — we recall the relations with Murnaghan's constants: $l = B + C$, $m = \frac{1}{2}A + B$ and $n = A$. In this context, it can be established [52] that:

$$
\begin{aligned}
\mathbf{S}_{NL}(\mathbf{u}_1, \mathbf{u}_2, 2) = {}& \lambda\text{tr}(\nabla\mathbf{u}_2)\nabla\mathbf{u}_1 + \mu\nabla\mathbf{u}_1(\nabla\mathbf{u}_2 + \nabla\mathbf{u}_2^T) \\
& + \lambda\text{tr}(\nabla\mathbf{u}_1)\nabla\mathbf{u}_2 + \mu\nabla\mathbf{u}_2(\nabla\mathbf{u}_1 + \nabla\mathbf{u}_1^T) \\
& + \lambda\text{tr}(\nabla\mathbf{u}_1^T\nabla\mathbf{u}_2)\mathbf{I} \\
& + \mu(\nabla\mathbf{u}_1^T\nabla\mathbf{u}_2 + \nabla\mathbf{u}_2^T\nabla\mathbf{u}_1) \\
& + 2C\text{tr}(\nabla\mathbf{u}_1)\text{tr}(\nabla\mathbf{u}_2)\mathbf{I} \\
& + B\text{tr}(\nabla\mathbf{u}_1)(\nabla\mathbf{u}_2 + \nabla\mathbf{u}_2^T) \\
& + B\text{tr}(\nabla\mathbf{u}_2)(\nabla\mathbf{u}_1 + \nabla\mathbf{u}_1^T) \\
& + \frac{B}{2}\text{tr}(\nabla\mathbf{u}_1\nabla\mathbf{u}_2 + \nabla\mathbf{u}_2\nabla\mathbf{u}_1 + 2\nabla\mathbf{u}_1^T\nabla\mathbf{u}_2)\mathbf{I} \\
& + \frac{A}{4}(\nabla\mathbf{u}_1\nabla\mathbf{u}_2 + \nabla\mathbf{u}_2\nabla\mathbf{u}_1 + \nabla\mathbf{u}_1^T\nabla\mathbf{u}_2^T \\
& + \nabla\mathbf{u}_2^T\nabla\mathbf{u}_1^T + \nabla\mathbf{u}_1^T\nabla\mathbf{u}_2 + \nabla\mathbf{u}_2^T\nabla\mathbf{u}_1 \\
& + \nabla\mathbf{u}_1\nabla\mathbf{u}_2^T + \nabla\mathbf{u}_2\nabla\mathbf{u}_1^T), \tag{A.4}
\end{aligned}
$$

in which $\mathbf{I}$ is the identity tensor of order 2 and rank 3. Eq. (A.4) and the results below are also valid for arbitrary variations of the elastic constants with depth. The case of an anisotropic medium requires to modify Eqs. (A.3) and (A.4) accordingly, but the further derivation still stands.

We now take the primary fields to be monochromatic and composed of a single mode each:

$$\mathbf{u}_1 = \text{Re}\left(A_1\mathbf{U}_1(z)e^{i(\omega_1 t - \mathbf{k}_1^T\mathbf{x})}\right), \tag{A.5a}$$

$$\mathbf{u}_2 = \text{Re}\left(A_2\mathbf{U}_2(z)e^{i(\omega_2 t - \mathbf{k}_2^T\mathbf{x})}\right), \tag{A.5b}$$

in which we assume $\omega_1 \geq \omega_2 > 0$. In Eqs. (A.5) the amplitudes A_1 and A_2 are defined depending on the normalization chosen for the modeshapes $\mathbf{U}_1$ and $\mathbf{U}_2$. This choice is postponed to Appendix B. The driving sources are composed of two parts, labeled with superscript $\pm$ to indicate respectively sum and difference interactions: $\mathbf{f}_{vol} = \text{Re}\left(\frac{1}{2}A_1A_2\mathbf{F}_{vol}^{\pm}e^{i[(\omega_1\pm\omega_2)t - (\mathbf{k}_1\pm\mathbf{k}_2)^T\mathbf{x}]}\right)$ (A_2 must be replaced by its conjugate A_2^* for the "−" case), and similarly for $\mathbf{f}_{surf}$. We recall (see

e.g. [53,54]) that when Fourier-transformed into the wavenumber domain $(x, y) \rightarrow (k_x, k_y)$, the causal Green's tensor of Eqs. (A.2) reads:

$$\mathbf{G}(z, z', t) = \sum_n g_n(t) \frac{\mathbf{U}_n(z)\mathbf{U}_n^H(z')}{\int_0^h \rho\|\mathbf{U}_n\|^2 dz}, \tag{A.6a}$$

$$g_n(t) = \mathcal{H}(t)\frac{\sin \omega_n t}{\omega_n}, \tag{A.6b}$$

where z' is the depth location of the impulsive source, ^{H} is the hermitian (or conjugate-transpose) operator, $\mathcal{H}$ is the Heaviside unitstep function, and $\mathbf{U}_n(\mathbf{k}, z)$ is the modeshape of the nth Lamb mode, associated with the eigen-angular frequency $\omega_n(\mathbf{k}) \geq 0$. Expressed over the Lamb modes of the plate, the resulting field is then of the form:

$$\mathbf{u}_{12} = \mathrm{Re}\left(\sum_n A_n^\pm(t)\mathbf{U}_n^\pm(z)e^{-i(\mathbf{k}_1 \pm \mathbf{k}_2)^T \mathbf{x}} \right), \tag{A.7}$$

with $\mathbf{U}_n^\pm = \mathbf{U}_n(\mathbf{k}_1 \pm \mathbf{k}_2)$. The superscripts $\pm$ and the substitution $A_2 \rightarrow A_2^*$ for the "−" case are from now on considered as implicit. The modal participation factors divided by the primary amplitudes are:

$$F_n(\mathbf{U}_1, \mathbf{U}_2, \mathbf{U}_n) = F_n^{vol} + F_n^{surf}, \tag{A.8a}$$

$$F_n^{vol} = \frac{1}{2}\int_0^h \mathbf{U}_n^H \mathbf{F}_{vol}(\mathbf{U}_1, \mathbf{U}_2)dz, \tag{A.8b}$$

$$F_n^{surf} = \frac{1}{2}\mathbf{U}_n^H \mathbf{F}_{surf}(\mathbf{U}_1, \mathbf{U}_2)|_0^h. \tag{A.8c}$$

As we are not interested in rigid body motions $\omega_n = 0$, the normalizing term in Eq. (A.6a) can be more conveniently written as the mean modal energy by multiplying by the halved squared angular frequency:

$$\mathcal{E}_n(\mathbf{U}_n, \omega_n) = \frac{1}{2}\omega_n^2 \int_0^h \rho\|\mathbf{U}_n\|^2 dz. \tag{A.9}$$

The temporal dependence is obtained by convolving the driving function $e^{i(\omega_1 \pm \omega_2)t}$ (assumed to be zero for $t < 0$) with the modal propagator $g_n(t)$. Combining terms, we arrive at:

$$\frac{A_n(t)}{A_1 A_2} = \frac{F_n}{2\mathcal{E}_n}\int_0^t e^{i(\omega_1 \pm \omega_2)\tau} \sin(\omega_n(t - \tau))\,\omega_n d\tau. \tag{A.10}$$

The sine function can be written as a sum of two exponentials, a form which exhibits two separate contributions: a first one associated with $-e^{-i\omega_n(t-\tau)}/2i$ which oscillates rapidly and cannot grow significantly, and a second one associated with $e^{i\omega_n(t-\tau)}/2i$ which can grow without limit if the resonance condition $\omega_n = \omega_1 \pm \omega_2$ is matched. We shall now neglect the former and approximate $A_n(t)$ by keeping only the latter:

$$\frac{A_n(t)}{A_1 A_2} \approx \begin{cases} i\gamma_{1,2,n}^{(t)} \frac{e^{i(\omega_1 \pm \omega_2)t} - e^{i\omega_n t}}{\omega_n - (\omega_1 \pm \omega_2)} & \text{if } \omega_n \neq \omega_1 \pm \omega_2, \\ \gamma_{1,2,n}^{(t)} t\, e^{i(\omega_1 \pm \omega_2)t} & \text{if } \omega_n = \omega_1 \pm \omega_2, \end{cases} \tag{A.11}$$

where we defined:

$$\gamma_{1,2,n}^{(t)} = \frac{\omega_n F_n}{4i\mathcal{E}_n}. \tag{A.12}$$

Finally, if we focus only on the resonance condition and slightly change the definition of $A_n(t)$ by pulling out the time-harmonic term $e^{i(\omega_1 \pm \omega_2)t}$ (*i.e.* we adopt the definition of Eq. (3a)), then Eq. (A.11) becomes Eq. (3b).

The coefficients $\gamma_{1,2,n}^{(t)}$ express how fast in time two given primary modes transfer energy into a third mode, and are defined up to an arbitrary factor that reflects the normalization chosen for the modes. They are analogous to what is often called "mixing power" in the literature, although referring to a transfer rate measured in space, along the propagation axis. The link between both forms is discussed below.

Correspondence with a representation in space. Let us compare the coupling coefficients as they appear in time and space representations. We now write the secondary field as:

$$\mathbf{u}_{12} = \mathrm{Re}\left(\sum_n A_n(\mathbf{x})\mathbf{U}_n(z)e^{i(\omega_1 \pm \omega_2)t} \right). \tag{A.13}$$

When the phase-matching condition is satisfied, it can be established [6, 9] that:

$$\frac{A_n(\mathbf{x})}{A_1 A_2} = \gamma_{1,2,n}^{(\mathbf{x})} \mathbf{q}^T \mathbf{x}\, e^{-i(\mathbf{k}_1 \pm \mathbf{k}_2)^T \mathbf{x}}, \tag{A.14}$$

where

$$\gamma_{1,2,n}^{(\mathbf{x})} = \frac{-i(\omega_1 \pm \omega_2)F_n}{4\mathcal{P}_{nn}}, \tag{A.15}$$

and $\mathbf{q} = (\mathbf{k}_1 \pm \mathbf{k}_2)/\|\mathbf{k}_1 \pm \mathbf{k}_2\|$ is the phase direction. In Eq. (A.15) $\mathcal{P}_{nn}$ is the mean power flux of mode n along $\mathbf{q}$:

$$\mathcal{P}_{nn} = \mathbf{q}^T \int_0^h \mathbf{P}_{nn}\, dz, \tag{A.16}$$

with $\mathbf{P}_{nn} = -\frac{1}{2}\mathrm{Re}\left(\mathbf{V}_n^H \mathbf{S}_L(\mathbf{U}_n)\right)$ the Poynting vector and $\mathbf{V}_n = i(\omega_1 \pm \omega_2)\mathbf{U}_n$ the velocity of the mode. Using the identity $\int_0^h \mathbf{P}_{nn}\, dz = c_{e,n}\mathcal{E}_n \mathbf{q}_{e,n}$, where $c_{e,n}$ is the energy (or group) velocity, $\mathbf{q}_{e,n}$ is a unit vector in the direction of the energy flux, and $\mathcal{E}_n$ is the time-average mechanical energy defined in Eq. (A.9), the ratio between both rates of transfer of energy can be obtained:

$$\frac{\gamma_{1,2,n}^{(t)}}{\gamma_{1,2,n}^{(\mathbf{x})}} = \frac{\mathcal{P}_{nn}}{\mathcal{E}_n} = c_{e,n}\mathbf{q}^T \mathbf{q}_{e,n}. \tag{A.17}$$

In other words, the transfer rate per unit space measured in the direction of energy flux, *i.e.* by setting $\mathbf{x} = x\mathbf{q}_{e,n}$ in Eq. (A.14), is equal to the transfer rate per unit time divided by the group velocity.

Appendix B. On the choice of normalization of the modeshapes

Amplitude. In scalar models of harmonic generation, the amplitudes of the components of the displacement field u are generally defined as $u = \sum_i A_i \cos \omega_i(t - x/c)$. If we stretch this representation into a transverse space dimension z (call it depth) over a distance h (call it thickness), we can introduce a trivial modeshape $U_i(z) = 1$ without changing the definition of A_i. The time-average and z-integrated mechanical energy carried by such harmonic wave with unit amplitude $A_i = 1$ is $\mathcal{E}_i = \frac{1}{2}\rho\omega_i^2 \int_0^h |U_i(z)|^2 dz = \frac{1}{2}\rho\omega_i^2 h$, where ρ is the density of the medium. Now, in the case of an elastic plate of density $\rho(z)$, with the purpose of dealing with coupling constants that have a similar meaning, it seems natural to require the modeshapes $\mathbf{U}_i(z)$ to be normalized such that their mechanical energy extends the scalar case:

$$\mathcal{E}_i = \frac{1}{2}\omega_i^2 \int_0^h \rho(z)\|\mathbf{U}_i(z)\|^2 dz = \frac{1}{2}\langle\rho\rangle \omega_i^2 h, \tag{B.1}$$

where $\langle\rho\rangle = \frac{1}{h}\int_0^h \rho dz$ is the average density. Note that if the medium is homogeneous $\rho(z) = \rho$, Eq. (B.1) simplifies to requiring $\frac{1}{h}\int_0^h \|\mathbf{U}_i(z)\|^2 dz = 1$.

Phase. Defining the phase of $\mathbf{U}_i$ is also necessary, although the choice is somewhat more arbitrary. In an isotropic plate, the in-plane and out-of-plane components of the modeshapes have a phase difference of $\pm\pi/2$, and either of them can be chosen to be pure real — this property applies to any layering of materials belonging to a class of anisotropy that includes orthotropy [53]. We then chose to require the in-plane components $U_{i,x}$ and $U_{i,y}$ to be pure-real. As for the $\pm$ sign that remains to be set, imposing a condition on the $U_{i,x}$ and $U_{i,y}$ components at $z = 0$ is convenient in that they can be simultaneously null only for $\mathbf{k} = \mathbf{0}$ — this is not the case for $U_{i,z}$ which is null for SH modes and cancels at $\omega/k = c_l$ for P-SV modes. We then decide to require $U_{i,x}|_{z=0}$ and $U_{i,y}|_{z=0}$ to be non-negative in the radial and azimuthal directions, *i.e.* $U_{i,x}|_{z=0} \geq 0$ and $U_{i,y}|_{z=0} \geq 0$ for $\mathbf{k}/\|\mathbf{k}\| = (1\,0\,0)^T$.

An example. Applied to the SH modes of an isotropic and homogeneous plate in the $\mathbf{k}/\|\mathbf{k}\| = (1\,0\,0)^T$ phase direction, this definition gives $\mathbf{U}_0 = (0\,1\,0)^T$ and $\mathbf{U}_i = \sqrt{2}\cos(i\,z\,\pi/h)\,(0\,1\,0)^T$ for $i > 0$.

Scaling of the coupling constants $\gamma_{1,2,3}^{(t)}$ *and* $\beta_{1,2,3}$ *with the plate thickness.* Normalized as described upper, $\mathbf{U}_i$ does not depend on h. Then, one can see from Eq. (A.9) that $\mathcal{E}_i/\omega_i$ scales as $\omega_i h$, that is, does not depend on h either. Furthermore, by changing to dimensionless coordinates $\mathbf{x} \rightarrow \tilde{\mathbf{x}} = \mathbf{x}/h$ and $\nabla \rightarrow \frac{1}{h}\nabla_{\tilde{\mathbf{x}}}$, we see from Eqs. (A.4) and (A.8) that F_n is proportional to $1/h^2$. We then see from Eqs. (A.12) and (4) that $\gamma_{1,2,3}^{(t)}$ scales as $1/h^2$ while $\beta_{1,2,3}$ is a constant that only depends on the mode triplet.

References

[1] P.B. Nagy, Fatigue damage assessment by nonlinear ultrasonic materials characterization, Ultrasonics 36 (1) (1998) 375–381, http://dx.doi.org/10.1016/S0041-624X(97)00040-1.

[2] K.H. Matlack, J.-Y. Kim, L.J. Jacobs, J. Qu, Review of second harmonic generation measurement techniques for material state determination in metals, J. Nondestruct. Eval. 34 (1) (2014) http://dx.doi.org/10.1007/s10921-014-0273-5.

[3] M. Deng, P. Wang, X. Lv, Experimental verification of cumulative growth effect of second harmonics of lamb wave propagation in an elastic plate, Appl. Phys. Lett. 86 (12) (2005) 124104, http://dx.doi.org/10.1063/1.1891295.

[4] C. Bermes, J.-Y. Kim, J. Qu, L.J. Jacobs, Experimental characterization of material nonlinearity using lamb waves, Appl. Phys. Lett. 90 (2) (2007) 021901, http://dx.doi.org/10.1063/1.2431467.

[5] C. Pruell, J.-Y. Kim, J. Qu, L.J. Jacobs, Evaluation of fatigue damage using nonlinear guided waves, Smart Mater. Struct. 18 (3) (2009) 035003, http://dx.doi.org/10.1088/0964-1726/18/3/035003.

[6] C.J. Lissenden, Nonlinear ultrasonic guided waves—principles for nondestructive evaluation, J. Appl. Phys. 129 (2) (2021) 021101, http://dx.doi.org/10.1063/5.0038340.

[7] M. Deng, Cumulative second-harmonic generation of lamb-mode propagation in a solid plate, J. Appl. Phys. 85 (6) (1999) 3051–3058, http://dx.doi.org/10.1063/1.369642.

[8] Y. Liu, V.K. Chillara, C.J. Lissenden, On selection of primary modes for generation of strong internally resonant second harmonics in plate, J. Sound Vib. 332 (19) (2013) 4517–4528, http://dx.doi.org/10.1016/j.jsv.2013.03.021.

[9] M. Hasanian, C.J. Lissenden, Second order harmonic guided wave mutual interactions in plate: Vector analysis, numerical simulation, and experimental results, J. Appl. Phys. 122 (8) (2017) 084901, http://dx.doi.org/10.1063/1.4993924.

[10] M. Hasanian, C.J. Lissenden, Second order ultrasonic guided wave mutual interactions in plate: Arbitrary angles, internal resonance, and finite interaction region, J. Appl. Phys. 124 (16) (2018) 164904, http://dx.doi.org/10.1063/1.5048227.

[11] Y. Ishii, K. Hiraoka, T. Adachi, Finite-element analysis of non-collinear mixing of two lowest-order antisymmetric rayleigh–lamb waves, J. Acoust. Soc. Am. 144 (1) (2018) 53–68, http://dx.doi.org/10.1121/1.5044422.

[12] Y. Ishii, S. Biwa, T. Adachi, Non-collinear interaction of guided elastic waves in an isotropic plate, J. Sound Vib. 419 (2018) 390–404, http://dx.doi.org/10.1016/j.jsv.2018.01.031.

[13] P. Blanloeuil, L. Rose, M. Veidt, C. Wang, Nonlinear mixing of non-collinear guided waves at a contact interface, Ultrasonics 110 (2021) 106222, http://dx.doi.org/10.1016/j.ultras.2020.106222.

[14] G.L. Jones, D.R. Kobett, Interaction of elastic waves in an isotropic solid, J. Acoust. Soc. Am. 35 (1) (1963) 5–10, http://dx.doi.org/10.1121/1.1918405.

[15] F.R. Rollins, Interaction of ultrasonic waves in solid media, Appl. Phys. Lett. 2 (8) (1963) 147–148, http://dx.doi.org/10.1063/1.1753818.

[16] L.H. Taylor, F.R. Rollins, Ultrasonic study of three-phonon interactions. i. theory, Phys. Rev. 136 (1964) A591–A596, http://dx.doi.org/10.1103/PhysRev.136.A591.

[17] F.R. Rollins, L.H. Taylor, P.H. Todd, Ultrasonic study of three-phonon interactions. ii. experimental results, Phys. Rev. 136 (1964) A597–A601, http://dx.doi.org/10.1103/PhysRev.136.A597.

[18] A.J. Croxford, P.D. Wilcox, B.W. Drinkwater, P.B. Nagy, The use of non-collinear mixing for nonlinear ultrasonic detection of plasticity and fatigue, J. Acoust. Soc. Am. 126 (5) (2009) EL117–EL122, http://dx.doi.org/10.1121/1.3231451.

[19] A. Demčenko, R. Akkerman, P. Nagy, R. Loendersloot, Non-collinear wave mixing for non-linear ultrasonic detection of physical ageing in pvc, NDT & E Int. 49 (2012) 34–39, http://dx.doi.org/10.1016/j.ndteint.2012.03.005.

[20] E.S. Furgason, V.L. Newhouse, Noncollinear three-phonon interactions in a multimode structure, J. Appl. Phys. 45 (5) (1974) 1934–1936, http://dx.doi.org/10.1063/1.1663524.

[21] N.G. Brower, W.G. Mayer, Noncollinear three-phonon interaction in an isotropic plate, J. Appl. Phys. 49 (5) (1978) 2666–2668, http://dx.doi.org/10.1063/1.325184.

[22] S.D. Holland, D.E. Chimenti, Air-coupled acoustic imaging with zero-group-velocity lamb modes, Appl. Phys. Lett. 83 (13) (2003) 2704–2706, http://dx.doi.org/10.1063/1.1613046.

[23] D. Clorennec, C. Prada, D. Royer, T.W. Murray, Laser impulse generation and interferometer detection of zero group velocity lamb mode resonance, Appl. Phys. Lett. 89 (2) (2006) 024101, http://dx.doi.org/10.1063/1.2220010.

[24] D. Clorennec, C. Prada, D. Royer, Laser ultrasonic inspection of plates using zero-group velocity lamb modes, IEEE Trans. Ultrason. Ferroelectr. Freq. Control 57 (5) (2010) 1125–1132, http://dx.doi.org/10.1109/tuffc.2010.1523.

[25] M. Cès, D. Clorennec, D. Royer, C. Prada, Thin layer thickness measurements by zero group velocity lamb mode resonances, Rev. Sci. Instrum. 82 (11) (2011) 114902, http://dx.doi.org/10.1063/1.3660182.

[26] G. Yan, S. Raetz, N. Chigarev, V.E. Gusev, V. Tournat, Characterization of progressive fatigue damage in solid plates by laser ultrasonic monitoring of zero-group-velocity lamb modes, Phys. Rev. Appl. 9 (2018) 061001, http://dx.doi.org/10.1103/PhysRevApplied.9.061001.

[27] D. Clorennec, C. Prada, D. Royer, Local and noncontact measurements of bulk acoustic wave velocities in thin isotropic plates and shells using zero group velocity lamb modes, J. Appl. Phys. 101 (3) (2007) 034908, http://dx.doi.org/10.1063/1.2434824.

[28] C. Prada, D. Clorennec, T.W. Murray, D. Royer, Influence of the anisotropy on zero-group velocity lamb modes, J. Acoust. Soc. Am. 126 (2) (2009) 620–625, http://dx.doi.org/10.1121/1.3167277.

[29] P. Ahn, O. Balogun, Elastic characterization of nanoporous gold foams using laser based ultrasonics, Ultrasonics 54 (3) (2014) 795–800, http://dx.doi.org/10.1016/j.ultras.2013.10.004.

[30] M. Thelen, N. Bochud, M. Brinker, C. Prada, P. Huber, Laser-excited elastic guided waves reveal the complex mechanics of nanoporous silicon, Nature Commun. 12 (1) (2021) http://dx.doi.org/10.1038/s41467-021-23398-0.

[31] S. Mezil, F. Bruno, S. Raetz, J. Laurent, D. Royer, C. Prada, Investigation of interfacial stiffnesses of a tri-layer using zero-group velocity lamb modes, J. Acoust. Soc. Am. 138 (5) (2015) 3202–3209, http://dx.doi.org/10.1121/1.4934958.

[32] Q. Xie, S. Mezil, P.H. Otsuka, M. Tomoda, J. Laurent, O. Matsuda, Z. Shen, O.B. Wright, Imaging gigahertz zero-group-velocity lamb waves, Nature Commun. 10 (1) (2019) http://dx.doi.org/10.1038/s41467-019-10085-4.

[33] R. Hodé, S. Raetz, J. Blondeau, N. Chigarev, N. Cuvillier, V. Tournat, M. Ducousso, Nondestructive evaluation of structural adhesive bonding using the attenuation of zero-group-velocity lamb modes, Appl. Phys. Lett. 116 (10) (2020) 104101, http://dx.doi.org/10.1063/1.5143215.

[34] C. Prada, D. Clorennec, D. Royer, Local vibration of an elastic plate and zero-group velocity lamb modes, J. Acoust. Soc. Am. 124 (1) (2008) 203–212, http://dx.doi.org/10.1121/1.2918543.

[35] C. Prada, D. Clorennec, D. Royer, Power law decay of zero group velocity lamb modes, Wave Motion 45 (6) (2008) 723–728, http://dx.doi.org/10.1016/j.wavemoti.2007.11.005.

[36] F. Bruno, J. Laurent, P. Jehanno, D. Royer, C. Prada, Laser beam shaping for enhanced zero-group velocity lamb modes generation, J. Acoust. Soc. Am. 140 (4) (2016) 2829–2838, http://dx.doi.org/10.1121/1.4965291.

[37] A. Gibson, J.S. Popovics, Lamb wave basis for impact-echo method analysis, J. Eng. Mech. 131 (4) (2005) 438–443, http://dx.doi.org/10.1061/(asce)0733-9399(2005)131:4(438).

[38] M. Ibanescu, S.G. Johnson, D. Roundy, Y. Fink, J.D. Joannopoulos, Microcavity confinement based on an anomalous zero group-velocity waveguide mode, Opt. Lett. 30 (5) (2005) 552, http://dx.doi.org/10.1364/ol.30.000552.

[39] V. Yantchev, L. Arapan, I. Katardjiev, V. Plessky, Thin-film zero-group-velocity lamb wave resonator, Appl. Phys. Lett. 99 (3) (2011) 033505, http://dx.doi.org/10.1063/1.3614559.

[40] E. Kausel, Number and location of zero-group-velocity modes, J. Acoust. Soc. Am. 131 (5) (2012) 3601–3610, http://dx.doi.org/10.1121/1.3695398.

[41] D. Yan, B.W. Drinkwater, S.A. Neild, Measurement of the ultrasonic nonlinearity of kissing bonds in adhesive joints, NDT & E Int. 42 (5) (2009) 459–466, http://dx.doi.org/10.1016/j.ndteint.2009.02.002.

[42] G. Shui, Y. sheng Wang, P. Huang, J. Qu, Nonlinear ultrasonic evaluation of the fatigue damage of adhesive joints, NDT & E Int. 70 (2015) 9–15, http://dx.doi.org/10.1016/j.ndteint.2014.11.002.

[43] P. Zabbal, G. Ribay, J. Jumel, Evaluation of metallic bonded plates with nonlinear ultrasound and comparison with destructive testing, NDT & E Int. 123 (2021) 102514, http://dx.doi.org/10.1016/j.ndteint.2021.102514.

[44] V.E. Gusev, A.M. Lomonosov, C. Ni, Z. Shen, Self-action of propagating and standing lamb waves in the plates exhibiting hysteretic nonlinearity: Nonlinear zero-group-velocity modes, Ultrasonics 80 (2017) 34–46, http://dx.doi.org/10.1016/j.ultras.2017.04.010.

[45] V. Gusev, Theory of non-collinear interactions of acoustic waves in an isotropic material with hysteretic quadratic nonlinearity, J. Acoust. Soc. Am. 111 (1) (2002) 80–94, http://dx.doi.org/10.1121/1.1382621.

[46] P. Blanloeuil, A. Meziane, C. Bacon, 2d finite element modeling of the non-collinear mixing method for detection and characterization of closed cracks, NDT & E Int. 76 (2015) 43–51, http://dx.doi.org/10.1016/j.ndteint.2015.08.001, URL https://www.sciencedirect.com/science/article/pii/S0963869515000833.

[47] R.T. Smith, R. Stern, R.W.B. Stephens, Third-order elastic moduli of polycrystalline metals from ultrasonic velocity measurements, J. Acoust. Soc. Am. 40 (5) (1966) 1002–1008, http://dx.doi.org/10.1121/1.1910179.

[48] J. Achenbach, Wave Propagation in Elastic Solids, in: North-Holland Series in Applied Mathematics and Mechanics, Elsevier, Amsterdam, 1975.

[49] S. Van der Walt, J.L. Schönberger, J. Nunez-Iglesias, F. Boulogne, J.D. Warner, N. Yager, E. Gouillart, T. Yu, Scikit-image: image processing in python, PeerJ 2 (2014) e453.

[50] M. Deng, Analysis of second-harmonic generation of lamb modes using a modal analysis approach, J. Appl. Phys. 94 (6) (2003) 4152–4159, http://dx.doi.org/10.1063/1.1601312.

[51] W. de Lima, M. Hamilton, Finite-amplitude waves in isotropic elastic plates, J. Sound Vib. 265 (4) (2003) 819–839, http://dx.doi.org/10.1016/s0022-460x(02)01260-9.

[52] V.K. Chillara, C.J. Lissenden, Interaction of guided wave modes in isotropic weakly nonlinear elastic plates: Higher harmonic generation, J. Appl. Phys. 111 (12) (2012) 124909, http://dx.doi.org/10.1063/1.4729554.

[53] E. Kausel, Thin-layer method: Formulation in the time domain, Internat. J. Numer. Methods Engrg. 37 (6) (1994) 927–941, http://dx.doi.org/10.1002/nme.1620370604.

[54] E. Ducasse, M. Deschamps, Time-domain computation of the response of composite layered anisotropic plates to a localized source, Wave Motion 51 (8) (2014) 1364–1381, http://dx.doi.org/10.1016/j.wavemoti.2014.08.003.